Spectroscopic characterization of Er^{3+}-doped Tl_3PbBr_5 for midinfrared laser applications

Alban Ferrier,* Matias Velázquez,† and Richard Moncorgé‡

Centre de Recherche sur les Ions, les Matériaux et la Photonique (CIMAP) UMR 6637 CEA-CNRS-ENSICAEN, Université de Caen, 6 Boulevard Maréchal Juin, 14050 Caen, France

(Received 9 November 2007; revised manuscript received 10 January 2008; published 21 February 2008)

This paper presents the optical and spectroscopic properties of a low-phonon-energy, moisture-resistant, and nonlinear $Er^{3+}:Tl_3PbBr_5$ single crystal. Though only weakly doped with Er^{3+} ions, centimeter-sized and good quality single crystals could be grown and analyzed. Excitation and emission spectra recorded at low temperature and crystal-field calculations agree with the existence of only one dominant Er^{3+} substitutional site. Anti-Stokes emission and excitation spectra as well as fluorescence decays and time-resolved emission and excited-state excitation spectra were recorded and analyzed to determine the different ways of populating the Er^{3+} excited levels and to provide all the necessary elements for an estimate of the laser potential of the considered material under diode laser pumping around 800 nm.

DOI: 10.1103/PhysRevB.77.075122 PACS number(s): 78.20.Bh, 78.40.Ha, 78.55.Hx, 71.70.Ch

I. INTRODUCTION

New crystalline hosts with low phonon frequencies, such as nonhygroscopic bromides and chlorides doped with trivalent rare-earth ions, are currently studied for their visible as well as midinfrared laser emissions.[1–7] In a recent work, we reported the crystal growth and the crystallographic and optical properties of pure, nonhygroscopic, and nonlinear Tl_3PbBr_5 (TPB) crystals.[8] The crystals exhibit the $P2_12_12_1$ space group, and the point symmetry of each of their nonequivalent Tl^+ and Pb^{2+} crystallographic sites is C_1. At room temperature, the structure displays two kinds of coordinance for the heavy metal cations: an eightfold one (with an average metal-bromide distance of 3.44 Å) and a sevenfold one (with average Tl-Br and Pb-Br distances of 3.36 and 3.14 Å, respectively), corresponding to three-dimensionally connected Archimedean antiprisms and pentagonal bipyramids.[9]

We also established that they are transparent from about 0.4 to more than 24 μm, and have a maximum Raman-active phonon mode frequency of about 138 cm^{-1}. Differential scanning calorimetry (DSC) measurements revealed that this compound undergoes a phase transition upon cooling, which, however, does not impede the growth of centimeter-sized single crystals. Then, by using a nanosecond pulsed laser at 1.38 μm, we also proved that powders obtained by crushing the crystals presented nonlinear properties with an effective nonlinear coefficient d_{eff} similar to that of KH_2PO_4 (KDP).

In this paper, we present results about the spectroscopic properties of Er^{3+}-doped Tl_3PbBr_5 single crystals. Doping with Er^{3+} ions is demonstrated, and very interesting broad and intense emission bands are shown in a wide spectral domain from the blue to the middle infrared. A series of spectroscopic measurements—low temperature excitation and emission spectra, room temperature fluorescence spectra and fluorescence decay times, up-conversion fluorescences—have been performed. These measurements allowed us to derive the energy level structure of the Er^{3+} ion electronic multiplets. These levels indicate the existence of only one major kind of Er^{3+} substitutional site, in good agreement with the crystal-field calculations. The various interstate excitation and emission spectra in the visible as well as in the infrared regions along with the fluorescence lifetime measurements were first used to calibrate the spectra in cross section unit, then to characterize the feeding and relaxation mechanisms of the various emitting levels following a particular type of excitation. Finally, the results have been analyzed to derive the best excitation conditions, for example, by using one and two pump photons around the diode laser wavelength of 800 nm, to possibly reach laser operation at various wavelengths, emphasizing those occurring in the midinfrared around 2.8 and 4.5 μm.

II. CRYSTAL GROWTH AND PHYSICAL PROPERTIES

Pure Tl_3PbBr_5 single crystals were first grown according to the standard Bridgman-Stockbarger process described in Ref. 8. The samples were ground to a powder and mechanically mixed with anhydrous and dry $ErBr_3$ powder in an agate mortar handled under a 3%-wet nitrogen-filled glovebox. The resulting admixture, poured into a quartz ampoule, was subsequently dried at 90 °C under 10^{-8} atm vacuum for 24 h, and thermally treated in stages of ~24 h at 220 and 280 °C under HBr gas atmosphere of 5*N* purity. The quartz crucible was finally sealed under Ar atmosphere (0.3 atm, 6*N* purity) and translated vertically at a speed of 1 mm h^{-1} in a two zone Bridgman-Stockbarger furnace with a 22 °C cm^{-1} thermal gradient. The initial powder mixture was doped with $ErBr_3$ at a nominal concentration of ~1 mol %. The real Er^{3+} content in the 70 mm long and 3.7 mm diameter single crystals was determined by inductively coupled plasma and Auger electron spectroscopy elemental analyses. The ion density in the terminal part of the single crystal was evaluated to be 2.4×10^{18} ions cm^{-3}.

Specific heat measurements were carried out between 265 and 425 K by means of DSC according to a procedure described in Ref. 10. In this temperature range, the C_p function (in units of J K^{-1} mol^{-1}) is well represented by a fourth order polynomial, namely,

$$C_p(T) = 1571.78 - 20.032T + 0.1049T^2 - 2.2335\times10^{-4}T^3 + 1.71\times10^{-7}T^4,$$

with a total relative error of ~12.5%. The knowledge of the

specific heat C_p function is useful not only for discussing the nature of the thermal phenomena occurring between room temperature and the melting point, but also for modeling the growth process (C_p enters the thermal inertia term in the heat balance equation as well as the melt interface boundary condition that accounts for the latent heat release) and the laser operation thermal management. We also carried out several hardness measurements by nanoindentation and comparison with a silica standard. The estimates obtained along and perpendicular to the growth direction all range between 6.7 and 7.3 GPa, which is less than the shear moduli of KPb_2Cl_5 single crystals [~11–14 GPa (Ref. 11)]. These values correspond to a hardness of about 2 Mohs, which is typical for chloride and bromide crystals. Consequently, the elastic strain energy that remains stored in the crystal upon substituting Er^{3+} cations for Tl^+ or Pb^{2+} ones may not account, alone, for the low Er^{3+} content achieved in these experiments. The refractive index of pure Tl_3PbBr_5 was finally evaluated by using two methods. The first one, based on the linearity and the additive law of the refractive index, enabled the determination of an average refractive index of Tl_3PbBr_5 from the well-known refractive indices of $PbBr_2$ and TlBr.[12] The calculated value at 650 nm is ~2.3. This average refractive index is close to the value of 2.23 ± 0.10, which is obtained at 632.8 nm (He-Ne laser) with a nonoriented crystal and by using the Brewster method. For calculations (see next parts), we decided to use the highest refractive index value to avoid overestimation of cross sections.

III. ROOM TEMPERATURE INFRARED EMISSION SPECTRA AND FLUORESCENCE DECAY TIME MEASUREMENTS

A. Experimental conditions

Continuous-wave emission spectra were registered at room temperature by exciting the sample with a tunable and continuous-wave (cw) Ti:sapphire laser (Coherent model 890). The emitting light was collected in an Oriel monochromator equipped with a 1200 grooves/mm grating blazed at 750 nm or a Jobin-Yvon HRS2 monochromator equipped with a 300 grooves/mm grating blazed at 2 μm for near- and midinfrared spectra, respectively. The signals were then detected either with a R928 Hamamatsu photomultiplier or an InSb (Judson model J10D) photodiode, and processed with a Stanford SR830 lock-in amplifier. All the spectra were obtained by using an appropriate filter and were corrected for the spectral response of the apparatus by using a blackbody reference source.

Fluorescence decays were obtained by exciting the sample with the 10 ns laser pulses from a wide-band optical parametric oscillator (GWU OPO model C-355) pumped by the third harmonic of a Q-switched Nd:YAG (yttrium aluminum garnet) laser (Spectron model 404G). The signals were then collected and dispersed into the above mentioned Oriel monochromator, equipped with different gratings, according to the considered emission wavelengths. They were detected with the same detectors as above and processed with a computer-interfaced Tektronix (TDS-350 model) oscilloscope.

TABLE I. Comparison between the experimental lifetimes of erbium doped bromide and chloride crystals.

	τ_{exp} (μs)		
Er^{3+} multiplet	$Er^{3+}:Tl_3PbBr_5$	$Er^{3+}:KPb_2Br_5$[a]	$Er^{3+}:KPb_2Cl_5$[b]
$^4I_{13/2}$	3800	4600	6200
$^4I_{11/2}$	3100	2100	3230
$^4I_{9/2}$	1800	1200 or 1900	2620
$^4F_{9/2}$	216	100	400
$(^4S_{3/2}, ^2H_{11/2})$	180	180	270
$^4F_{7/2}$	70	85	10
$(^4F_{5/2}, ^4F_{3/2})$	110	?	130
$^2H_{9/2}$	2.9	34	120

[a]Reference 2.
[b]References 13 and 14.

B. Experimental results

We determined first the lifetimes of most of the Er^{3+} excited multiplets. All the measured fluorescence decays were found exponential with the time constants reported in Table I. Time constants from another bromide[5] and a chloride[13,14] are also presented in this table for comparison. In the two bromide crystals, the Er^{3+} lifetimes have about the same values. This observation is not surprising since it is expected from their crystal structures that the rare-earth active ions take up the same kind of low symmetry site. However, a large discrepancy is observed for the $^2H_{9/2}$ multiplet since its lifetime in Er:TPB is 10 times shorter than in Er:KPB. A possible explanation is that a relaxation path takes place, in the case of Er:TPB, from this multiplet to some charge transfer band involving the Tl^+ ions. In spite of lower phonon energies, thus, in principle, of reduced multiphonon relaxations, the lifetimes found in Er:TPB are shorter, except for the $^4F_{7/2}$ multiplet, than the lifetimes found in Er:KPC.[13,14] This probably arises from an increase of the $4f$-$4f$ transition probabilities due to the decreasing energy and the increasing admixture of the wave functions with the lowest energy $4f^{10}5d$ band along the Cl-Br-I halide series.[15] On the other hand, for the $^4F_{7/2}$ multiplet which is closer to the next energy level lying below it than the other multiplets, the longer lifetime found in the case of the bromide compared to the chloride is simply due to a lower multiphonon relaxation.

The room temperature emission cross-section spectra of Er:TPB are shown in Fig. 1. Emission spectra were transformed in cross-section spectra by using the well-known Fuchtbauer-Ladenburg method.[16,17] This method originating from the relation between the Einstein coefficients allows a direct determination of emission cross sections from fluorescence spectra by using the formula:

$$\sigma_{SE}(\lambda) = \frac{\lambda^5 \beta I(\lambda)}{8\pi c n^2 \tau_{rad} \int \lambda I(\lambda) d\lambda}. \quad (1)$$

In this expression, $I(\lambda)$ is the emission intensity, β is the branching ratio of the considered intermultiplet transition,

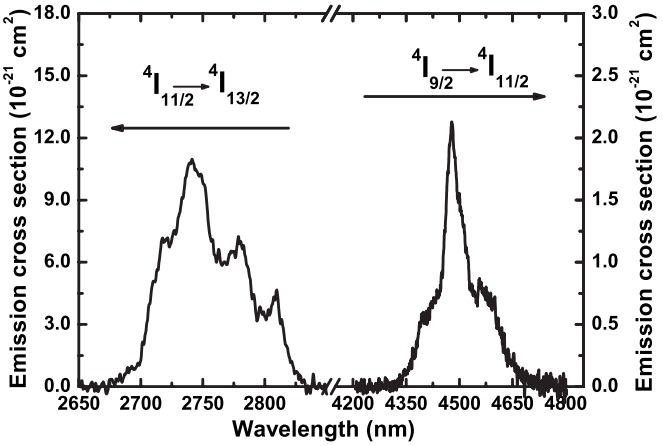

FIG. 1. Room temperature emission cross section of the two midinfrared luminescences of $Er^{3+}:Tl_3PbBr_5$.

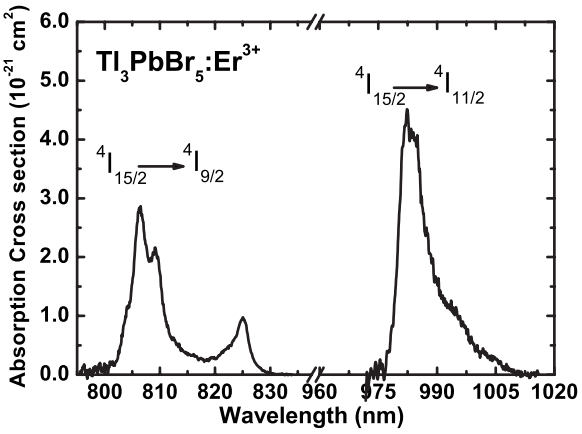

FIG. 2. Room temperature absorption spectra of $Er^{3+}:Tl_3PbBr_5$ determined by using both Fuchtbauer-Ladenburg and reciprocity relations.

τ_{rad} is the radiative lifetime for each specific emitting level, c is the speed of light, and n the index of refraction. Whenever it made sense, τ_{rad} was replaced by τ_f, the experimentally measured fluorescence lifetime of the considered emitting level, as reported in Table I. Indeed, our sample incorporated not enough Er^{3+} ions to register as many absorption bands as would be necessary to perform a significant and reliable Judd-Ofelt analysis. This approximation is only valid and was only used for emitting levels lying sufficiently above a next low-lying one to assume negligible nonradiative multiphonon relaxation. Then, emission cross-section spectra could be transformed into absorption cross-section spectra by using the reciprocity relation, as given by[16]

$$\sigma_{abs}(\lambda) = \sigma_{SE}(\lambda)\frac{Z_{up}}{Z_{low}}\exp\left[-\frac{1}{k_B T}\left(E_{ZL} - \frac{hc}{\lambda}\right)\right] \qquad (2)$$

where k_B and h stand for the Boltzman and the Planck constants, respectively; Z_u and Z_l for the partition functions for the high- and low-lying energy multiplets; and E_{ZL} represents what is called the zero-line (ZL) energy, i.e., the energy separation between the lowest Stark components of each multiplet. The partition functions and ZL energies of the considered transitions can be easily derived by using the energy level positions reported in Table II (see next part).

Figure 1 gathers the emission cross-section spectra associated with the two midinfrared $^4I_{11/2} \rightarrow {}^4I_{13/2}$ and $^4I_{9/2} \rightarrow {}^4I_{11/2}$ emission transitions located around 2750 and 4500 nm, respectively, as obtained after 800 nm excitation. Such large emission cross sections have the same order of magnitude as in the now well-known Er:KPC laser crystal,[1,2] which indicates that Er:TPB could also be a good candidate for midinfrared laser operation. Furthermore, absorption bands (see Fig. 2) are broad and well adapted to diode laser pumping.

IV. LOW TEMPERATURE SPECTRAL DATA AND CRYSTAL-FIELD CALCULATIONS

A. Experimental conditions

The $Er^{3+}:Tl_3PbBr_5$ sample (3 mm long, 4 mm diameter) was clamped onto the copper cold finger of a closed circuit

TABLE II. Comparison of observed and calculated low-lying Stark sublevel energies of $Er^{3+}:Tl_3PbBr_5$ and calculated positions of upper-lying ones (column 4: partition functions of respective multiplets).

Er^{3+} multiplet	Experimental results	Crystal field calculation	Partition function Z_i
$^4I_{15/2}$	0, 24, 36, 54, 91, 145, 162, 218,	0, 23, 42, 56, 93, 144, 162, 210	5.434
$^4I_{13/2}$	6510, 6533, 6538, 6571, 6600, 6618, 6656	6512, 6529, 6538, 6568, 6603, 6617, 6658	5.313
$^4I_{11/2}$	10157, 10178, 10194, 10202, 10208, 10236	10163, 10170, 10185, 10201, 10215, 10241	5.153
$^4I_{9/2}$	12372, 12417, 12436, 12458, 12472	12365, 12416, 12430 12461, 12482	3.714
$^4F_{9/2}$		15200, 15209, 15242 15265, 15311	4.093
$^4S_{3/2}$		18262, 18303	1.817
$^2H_{11/2}$		18995, 19018, 19025, 19053, 19069, 19076	4.896
$^4F_{7/2}$		20288, 20320, 20347, 20365	3.301
$^4F_{5/2}$		22007, 22030, 22041	2.744
$^4F_{3/2}$		22381, 22434	1.775
$^2H_{9/2}$		24373, 24416, 24433, 24460, 24474	3.835

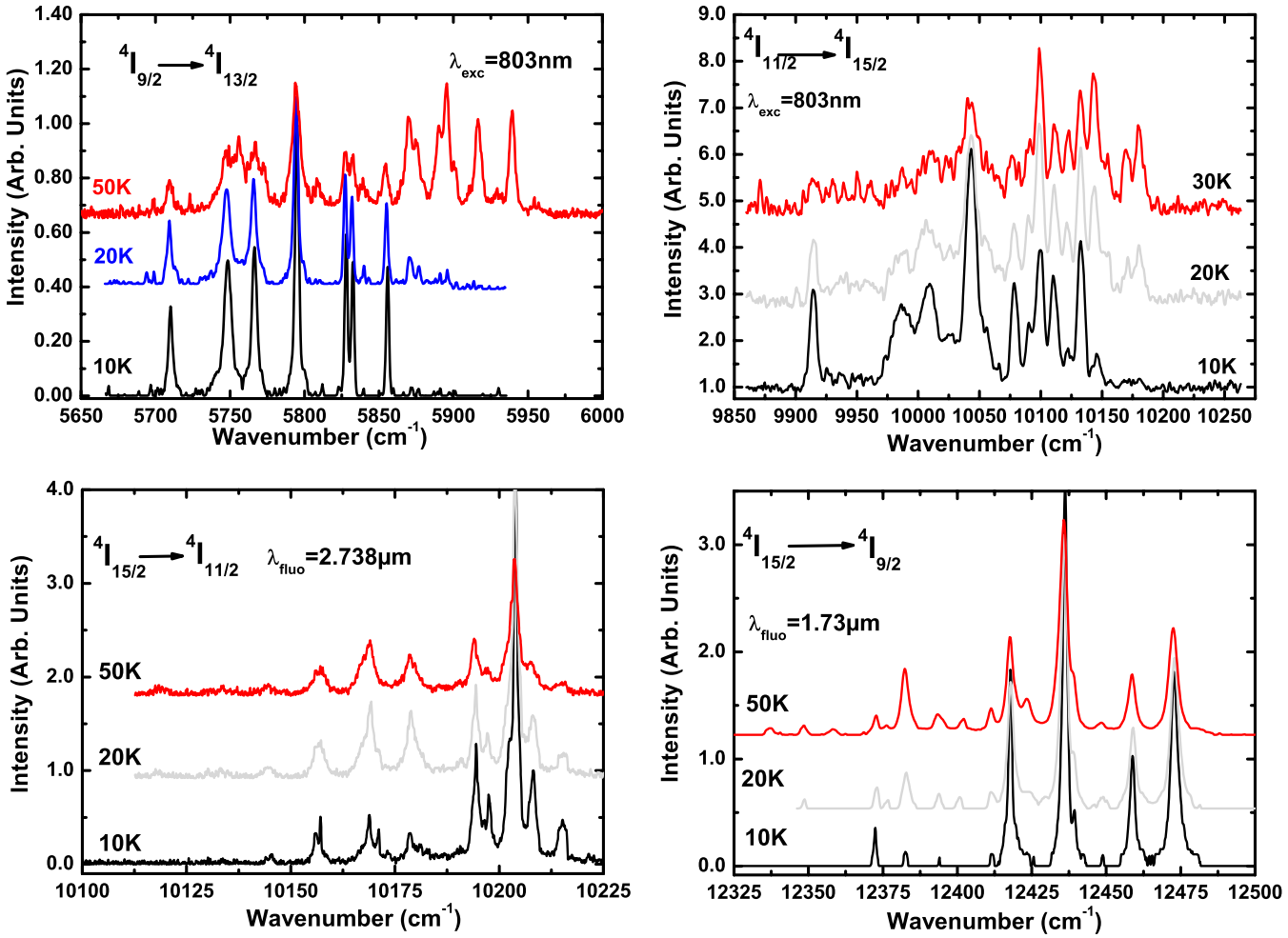

FIG. 3. (Color online) Low temperature emission or excitation spectra of Er^{3+}:$Tl_3PbBr_5{}^{3+}$ used for the determination of energy levels.

ADP helium cryostat and its temperature could be lowered and regulated down to 10 K. Continuous-wave emission and excitation spectra were registered at low temperature by exciting the sample with the same tunable and continuous-wave Ti:sapphire laser as mentioned above.

B. EXPERIMENTAL RESULTS

For rare-earth ions with an odd number of electrons, a low symmetry crystal field splits the free-ion energy levels with a total angular momentum J into $[(J+1)/2]$ Stark sublevels.[18] Since at low temperature the transition lines are sharp enough to distinguish between each inter-Stark sublevel transition, it is possible to determine the number of contributing Er^{3+} sites by counting the number of lines. For instance, for one kind of low symmetry substitutional site, five lines are expected in the excitation spectrum of level $^4I_{9/2}$, which is, indeed, observed and displayed in Fig. 3. This kind of measurements was performed for the four first excited multiplets and enabled the determination of their energy sublevels, as reported in Table II. If it looks clear that only one kind of Er^{3+} sites contributes to the spectra, several types of lattice defects can be involved. Indeed, the substitution of Er^{3+} ions for heavy metal cations can lead to the formation of either (1) $Er_{Tl}^{\bullet\bullet} + V_{Pb}''$, (2) $Er_{Tl}^{\bullet\bullet} + 2V_{Tl}'$, (3) $Er_{Tl}^{\bullet\bullet} + 2Br_i'$, (4) $Er_{Tl}^{\bullet\bullet} + 2Pb_{Pb}'$, (5) $2Er_{Pb}^{\bullet} + V_{Pb}''$, (6) $Er_{Pb}^{\bullet} + V_{Tl}'$, (7) $Er_{Pb}^{\bullet} + Br_i'$, or (8) $Er_{Pb}^{\bullet} + Pb_{Pb}'Er_{Pb}^{\bullet} + Pb_{Pb}'$ point defects to ensure electroneutrality of the crystal lattice (Kröger-Vink's notation has been used). Defects (3) and (7) require large enough interstitial voids in the crystal structure to accommodate bromide anions as well as a brominating atmosphere. Owing to the density of the crystal packing, the former condition is not easily verified. The Ellingham diagram clearly shows that charge compensation defects (4) and (8) are not thermodynamically favored under HBr gas atmosphere.[8] As the differences between the seven- and eightfold ionic radii and dipolar polarizabilities between the Er^{3+} and Pb^{2+} cations are smaller than those between the Er^{3+} and Tl^{+} cations, we would think *a priori* that Er^{3+} ions preferentially occupy Pb^{2+} sites. However, as the difference in Pauling electronegativity between Er^{3+} and Pb^{2+} cations is higher than that between the Er^{3+} and Tl^{+} cations, and all the cationic crystallographic sites exhibit seven (eight)fold coordination polyhedra, defects (1) and (2) should not be entirely discarded at this time. Defect (5) corresponds to the nominal formula $Tl_3Pb_{1-3x/2}Er_xBr_5$, defects (1) and (6) to the composition $Tl_{3-x}Pb_{1-x}Er_xBr_5$, and defect (2) to the composition $Tl_{3-3x}PbEr_xBr_5$.

C. Crystal-field calculations

In this analysis, we used the energy levels of 11 multiplets $^{2S+1}L_J$ of the $4f^{11}$ (Er^{3+}) electronic configuration. They include the 26 crystal-field levels of the $^4I_{15/2}$, $^4I_{13/2}$, $^4I_{11/2}$, and $^4I_{9/2}$ multiplets, and the 7 centroids of the $^4F_{9/2}$, $^4S_{3/2}$, $^2H_{11/2}$, $^4F_{7/2}$, $^4F_{5/2}$, $^4F_{3/2}$, and $^2H_{9/2}$ multiplets, as determined in the previous section. These experimental level energies were used as the input data in a parametrized Hamiltonian. The free-ion parameters chosen for our calculations were obtained from Carnall *et al.*[19] For Er^{3+}, in aqueous solution the parameters (all in cm^{-1}) are

$$E^{(1)} = 6769.9, \quad E^{(2)} = 32.388, \quad E^{(3)} = 646.62,$$

$$\xi = 2380.7, \quad \alpha = 18.347, \quad \beta = -509.28, \quad \gamma = 649.71.$$

The crystal-field potential at the Er^{3+} ion sites was assumed to be of C_2 symmetry, and the Hamiltonian expressed as

$$H_{CF} = \sum_{k,q} B_q^k \sum_i C_q^k(i), \tag{3}$$

where the B_q^k's are the crystal-field parameters and C_q^k is a spherical tensor of rank k and order q. The second sum is over $i=1-N$, where N is the number of electrons ($4f^{11}$).

In order to initiate the calculations, we used the set of crystal-field parameters given by Cascales *et al.*[20] in the case of Eu^{3+}-doped KPb_2Cl_5 in Cs/C_2 site symmetry. The Er^{3+} parameters were deduced from the Eu^{3+} ones by using the relations

$$B_q^k(Er^{3+}) = \frac{\rho_k(Er^{3+})}{\rho_k(Eu^{3+})} B_q^k(Eu^{3+}), \tag{4}$$

the radial factors being given by Morrison and Leavitt.[21] The set of B_q^k parameters was then varied with a least-squares procedure based on the 26 energy levels of the above mentioned multiplets. The B_q^k which gave the best fit to the experimental energy levels, with a rms value of 7.2 cm^{-1}, are

$$B_0^2 = 302.6, \quad B_2^2 = 70.1, \quad B_0^4 = 299.9,$$
$$\mathrm{Re}\, B_2^4 = 550.9, \quad \mathrm{Im}\, B_2^4 = -160.2,$$

$$\mathrm{Re}\, B_4^4 = 368.5, \quad \mathrm{Im}\, B_4^4 = 112.6, \quad B_0^6 = -53.5,$$
$$\mathrm{Re}\, B_2^6 = 104.1, \quad \mathrm{Im}\, B_2^6 = -17.9,$$

$$\mathrm{Re}\, B_4^6 = 27.3, \quad \mathrm{Im}\, B_4^6 = -89.7, \quad \mathrm{Re}\, B_6^6 = -26.7,$$
$$\mathrm{Im}\, B_6^6 = -46.1.$$

The calculated and experimental energy levels are reported in Table II.

As pointed out recently by Rudowicz and Quin,[22] it is very difficult to compare the crystal-field parameters from different studies for low symmetry sites. Nevertheless, it is possible to use, for comparison, the crystal-field strength N_v, as first introduced by Auzel and Malta:[23]

$$N_v = \sqrt{\sum_{k,q} (B_q^k)^2 \left(\frac{4\pi}{2k+1}\right)}. \tag{5}$$

The crystal-field strength of our bromide is found equal to about 1326 cm^{-1}. This value is relatively low if we compare it to that found in KPb_2Cl_5 ($N_v = 1787$ cm^{-1}).[13] This is an important point because energy-transfer microparameters depend on spectral overlaps and it is expected that such overlaps increase for large crystal-field strengths (see next part).

V. ANTI-STOKES EXCITATION AND EMISSION PROCESSES

A. Experimental conditions

cw anti-Stokes emission and excitation spectra were registered at room temperature by exciting again the sample at approximately 800 nm with a tunable and cw Ti:sapphire laser (Coherent model 890). Fluorescence spectra were corrected for the spectral response of the apparatus by using a calibrated tungsten-halogen lamp source, and excitation spectra were corrected for the spectral variation of the Ti:sapphire laser intensity by dividing the signals by this intensity, as given by a standard calorimeter, or by the square of this intensity, depending on the involved excitation process. Time-resolved emission spectra registered around 800 nm and fluorescence decay of $^4S_{3/2}$ (after excitation at 800 nm) were obtained by exciting the sample with the 10 ns laser pulses from a wide-band optical parametric oscillator (GWU OPO model C-355) pumped by the third harmonic of a Q-switched Nd:YAG laser (Spectron model 404G). Emission signals were dispersed with a 25 cm focal length Oriel monochromator equipped with a 1200 grooves/mm grating blazed at 750 nm, detected with a Hamamatsu R5108 photomultiplier, and fed into a computer-interfaced Tektronix (TDS-350 model) oscilloscope. All these time-resolved spectra were recorded at both short and long time delays after the exciting laser pulses to distinguish between overlapping emission components. Then, these time-resolved emission spectra were transformed in cross-section spectra by using the classical Fuchtbauer-Ladenburg method. The next and final step of this investigation consisted in transforming the derived emission cross-section spectra in absorption cross sections by using the above described reciprocity method. For the long lived anti-Stokes fluorescences, use was made of the Ti:sapphire laser mentioned above, coupled to an acousto-optic modulator.

B. Anti-Stokes emission and excitation spectra

As already described for a large variety of materials (oxide, fluoride, chloride, and bromide) efficient green anti-Stokes fluorescences are observed in the case of Er^{3+} under 800 nm excitation (see, for example, Refs. 24–27). Despite the low concentration of Er^{3+}, we observed anti-Stokes emissions after 800 nm excitation (Fig. 4). As in the case of Er:KPC ($Er^{3+}:KPb_2Cl_5$), anti-Stokes luminescences originate from levels $^2H_{9/2}$, $^4F_{3/2}$, $^4F_{5/2}$, $^4F_{7/2}$, $^2H_{11/2}$, and $^4S_{3/2}$.[13,25] Nevertheless, some differences exist between $Er^{3+}:KPb_2Cl_5$ and $Er^{3+}:Tl_3PbBr_5$. First, it was not possible

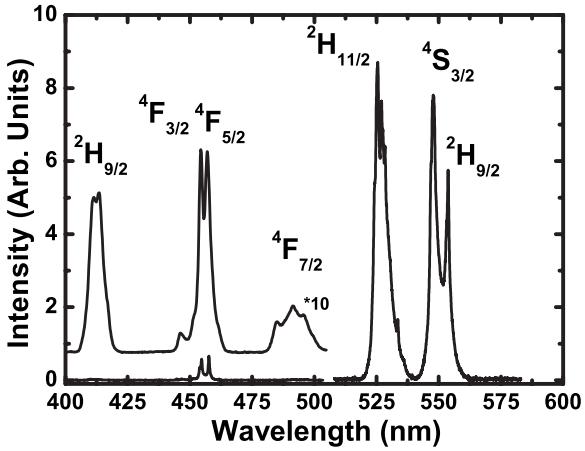

FIG. 4. Anti-Stokes luminescence spectra of Er^{3+}:$Tl_3PbBr_5{}^{3+}$ obtained at 295 K after excitation at 804 nm.

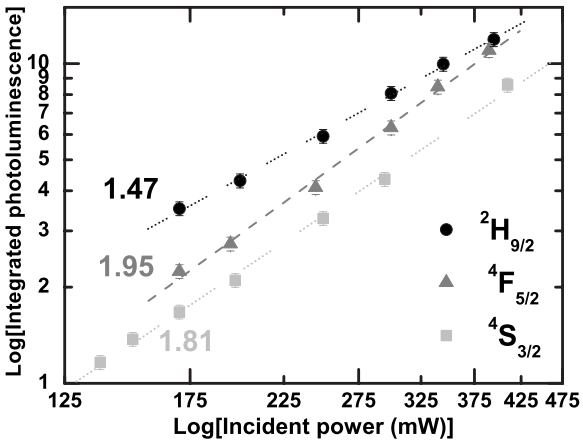

FIG. 5. Logarithmic plot of the integrated intensities of the up-converted emission coming from levels $^2H_{9/2}$, $^4F_{5/2}$, and $^4S_{3/2}$ obtained at 295 K after 804 nm excitation.

to observe any anti-Stokes luminescence from the $^4G_{11/2}$ level in the bromide crystal. Furthermore, the ratios between the intensities of the anti-Stokes fluorescences are different. This is the case, for example, of the anti-Stokes luminescences from the levels $^2H_{9/2}$ and ($^4F_{3/2}$,$^4F_{5/2}$) since they have about the same intensities in Er:TPB, whereas the anti-Stokes luminescence from level $^2H_{9/2}$ dominates in the case of Er:KPC. These differences probably come from a modification of the up-conversion probabilities resulting from different crystal-field splittings (which are smaller in the case of bromide crystals) and, in the case of phonon-assisted up-conversion energy transfers, from lower phonon energies in bromides than in chlorides.

To determine the exact nature of the mechanisms responsible for these up-conversion luminescences, we studied first the evolution of their intensities as a function of the excitation pump power. Indeed, at least in the low power limit (i.e., far from saturation), these intensities should scale as P^n where P stands for the pump power and n represents the number of photons involved in the excitation process. Up-conversion emission intensities were, thus, registered at 412 nm ($^2H_{9/2}$), 455 nm ($^4F_{5/2}$), and 550 nm ($^4S_{3/2}$) for different pump powers and plotted (see Fig. 5) with double logarithmic scales. For emissions coming from levels $^4F_{5/2}$ and $^4S_{3/2}$, the fluorescence intensities vary almost quadratically, which means two photon excitation processes. On the contrary, the slope for the $^2H_{9/2}$ anti-Stokes emission intensity significantly differs by a factor 2. This discrepancy could be attributed to some competition between energy transfer and radiative emission.[28,29]

Then, to further investigate the involved up-conversion processes, excitation spectra of the anti-Stokes luminescences were recorded. Indeed, two different kinds of excitation spectra are expected in the case of energy-transfer up-conversion[30] (ETU or APTE) or of excited state absorption (ESA). In the case of ETU, the excitation spectrum is similar to the ground-state absorption (GSA) spectrum and the spectral features are narrower as the number of photons involved in the up-conversion process is larger.[31] On the contrary, in the case of ESA, the excitation spectrum is a convolution of a GSA and ESA spectra, and different spectral features appear.

Such excitation spectra obtained by tuning the excitation wavelength from about 790 to 835 nm and by monitoring each of the detected anti-Stokes emissions are reported in Fig. 6. We focused our attention on the up-conversion excitation processes leading to the emissions coming from all the levels $^2H_{9/2}$, $^4F_{5/2}$, $^4F_{7/2}$, and $^4S_{3/2}$, assuming the pairs of

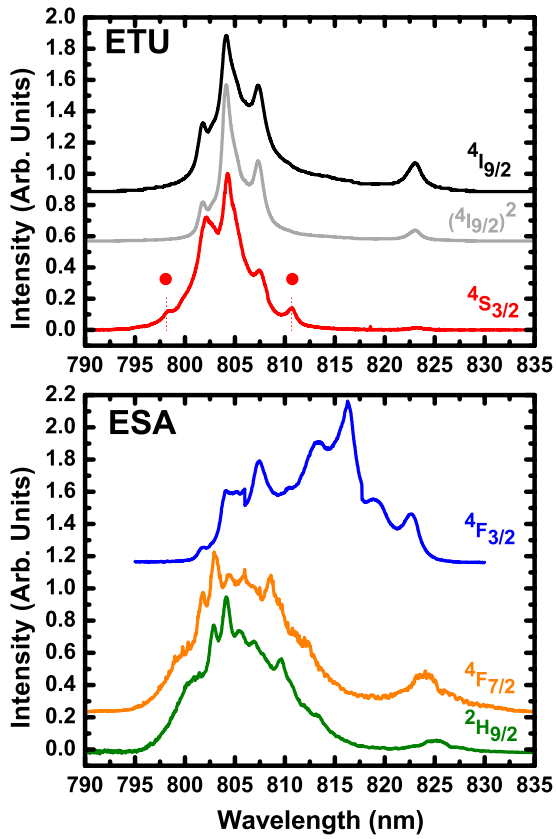

FIG. 6. (Color online) Excitation spectra (registered around 800 nm) of the up-converted luminescence of Er^{3+}:Tl_3PbBr_5. Also reported, for comparison, are the excitation spectrum of the $^4I_{9/2}$ luminescence and the square of it (all the spectra are normalized to their peak intensity and are vertically translated for better reading).

levels $(^4F_{3/2}, ^4F_{5/2})$ and $(^2H_{11/2}, ^4S_{3/2})$ being thermalized at room temperature. As indicated by the $^4I_{15/2} \rightarrow ^4I_{9/2}$ ground-state excitation spectrum (GSA), also reported in Fig. 6 for the sake of clarity, and the energy level positions reported in Table II, it is clear that the $^4S_{3/2}$ excitation spectrum is closely related, at least between 795 and 815 nm, to the $^4I_{9/2}$ absorption spectrum. It means that the involved up-conversion excitation process is very likely the nearly resonant ETU processes written as follows:

$$(^4I_{9/2}, ^4I_{9/2}) \rightarrow (^4I_{13/2}, ^4S_{3/2}) \quad \text{[process (I)]},$$

$$(^4I_{13/2}, ^4I_{9/2}) \rightarrow (^4I_{15/2}, ^4S_{3/2}) \quad \text{[process (II)]}.$$

Nevertheless, the excitation spectrum of $^4S_{3/2}$ presents additional features and is significantly broader than the square of the $^4I_{9/2}$ excitation spectrum. This indicates that another process takes place. In order to account for such an unexpected broadening, an additional ESA process is proposed

$$^4I_{13/2} + h\nu \rightarrow ^2H_{11/2} \text{ followed by}$$
$$(^2H_{11/2}, ^4S_{3/2}) \text{ thermalization} \quad \text{[process (III)]}.$$

The situation is clearly different for the excitation spectra of the anti-Stokes luminescences coming from the $(^4F_{3/2}, ^4F_{5/2})$, $^4F_{7/2}$, and $^2H_{9/2}$ levels since the spectra clearly differ from the $^4I_{9/2}$ excitation spectrum. The $(^4F_{3/2}; ^4F_{5/2})$ anti-Stokes fluorescence excitation spectrum presents a complex structure with a maximum around 815 nm, far from the main absorption peak characteristic of the $^4I_{9/2}$ GSA spectrum. To explain such a result, an additional ESA process is proposed

$$^4I_{11/2} + h\nu \rightarrow ^4F_{3/2} \text{ followed by}$$
$$(^4F_{3/2}, ^4F_{5/2}) \text{ thermalization} \quad \text{[process (IV)]}.$$

This up-conversion mechanism appears as the most efficient process but, in agreement with a previous study on Er:KPC (Ref. 13) and with the results of the energy level calculations, the two following ETU processes also probably occur:

$$(^4I_{9/2}, ^4I_{11/2}) \rightarrow (^4I_{15/2}, ^4F_{3/2}) \text{ followed by}$$
$$(^4F_{3/2}, ^4F_{5/2}) \text{ thermalization} \quad \text{[process (V)]},$$

$$(^4I_{9/2}, ^4I_{11/2}) \rightarrow (^4F_{3/2}, ^4I_{15/2}) \text{ followed by}$$
$$(^4F_{3/2}, ^4F_{5/2}) \text{ thermalization} \quad \text{[process (VI)]}.$$

In the case of the $^2H_{9/2}$, the excitation spectrum also presents a complicated structure. As for the case of $(^4F_{3/2}, ^4F_{5/2})$, this experimental observation suggests that the following ESA process takes places:

$$^4I_{9/2} + h\nu \rightarrow ^2H_{9/2} \quad \text{[process (VII)]}.$$

The excitation spectrum, however, occurs in the same domain and has some similarity with the $^4I_{9/2}$ GSA spectrum, for example, around 805 nm. This is the reason why it is also proposed the ETU process:

$$(^4I_{9/2}, ^4I_{9/2}) \rightarrow (^4I_{15/2}, ^2H_{9/2}) \quad \text{[process (VIII)]}.$$

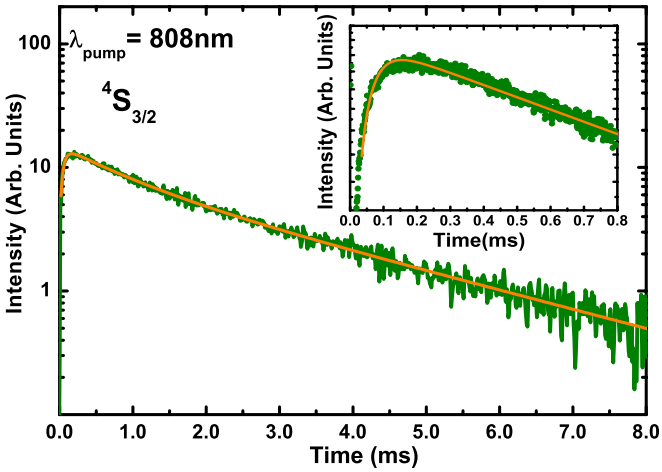

FIG. 7. (Color online) Room temperature anti-Stokes fluorescence transients from level $^4S_{3/2}$ after an 800 nm excitation.

The excitation spectrum of the $^4F_{7/2}$ multiplet is very similar to the excitation spectrum of the $^2H_{9/2}$ multiplet. Its structure, thus, indicates that some ESA process also takes place. According to the energy level positions, however, no ESA transition around 800 nm can reach this $^4F_{7/2}$ level directly. In fact, ESA could take place either from the $^4I_{9/2}$ or the $^4I_{11/2}$ level up to the $^2H_{9/2}$ or the $(^4F_{3/2}, ^4F_{5/2})$ multiplet from which the excitation relaxes down to level $^4F_{7/2}$. The first process seems much more likely, however, than the second one since the resulting excitation spectrum is much more similar to the $^2H_{9/2}$ than to the $^4F_{5/2}$ excitation spectrum and also because of more favorable branching ratios.[14]

C. Fluorescence decay measurements and analysis

In the case of energy transfer, time-resolved measurements following pulsed laser excitation can be useful to distinguish between ETU and ESA processes. Indeed, ESA takes place during the excitation pulse, whereas ETU could also operate at long time delays after the excitation laser pulse. This is the reason why in the first case the decay curve is similar to the decay curve obtained under resonant excitation, whereas in the case of ETU, the decay curve presents a rise followed by a nonexponential decay with a time constant which may be much longer than the time constant obtained for direct excitation (feeding process).

The fluorescence transient resulting from the anti-Stokes emission coming from level $^4S_{3/2}$ after 808 nm excitation is shown in Fig. 7. The decay curve presents a rise time and a nonexponential decay. Such a decay curve thus indicates that, for this excitation wavelength and this emitting level, an ETU process is taking place. This decay curve was fitted (red curve in Fig. 7) using the already discussed[13,25] theoretical expression:

$$n(t) = (b + c)e^{t/\tau_1} + be^{-t/\tau_2} - ce^{-t/\tau_3}$$

with the time constants $\tau_1 \approx 40\ \mu s$, $\tau_2 \approx 930\ \mu s$, and $\tau_3 \approx 2.8$ ms.

These long time constant values seem consistent with the near resonant processes (I) and (II). For instance, τ_2 is, in-

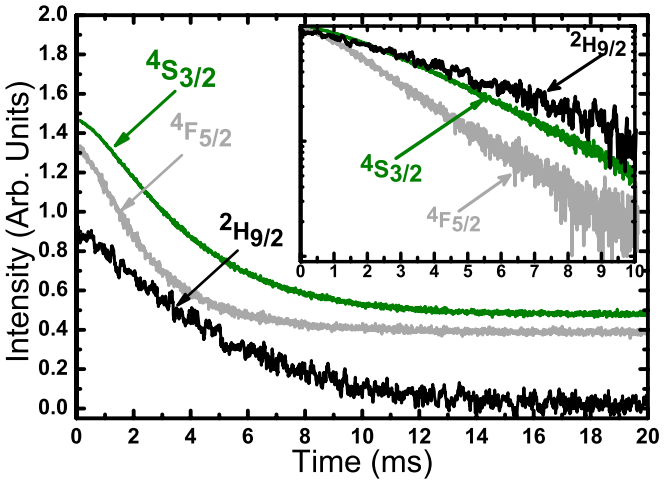

FIG. 8. (Color online) Temporal behavior of the up-conversion luminescence obtained for a 2 ms pulse excitation at 805 nm (decay curves normalized and vertically translated). The inset shows the same decay curves with a semilogarithmic scale.

deed, about half the $^4I_{9/2}$ lifetimes (Table I), which is consistent with the cross relaxation (I). Interpretation of time constant τ_3 is more delicate, but seems in agreement with the mechanism (II) because the multiplet $^4I_{13/2}$ presents a long lifetime [$^4I_{13/2}$ is mainly populated via radiative transfer from $^4I_{9/2}$ and by energy transfer (I)] and a non-negligible population [$\beta(^4I_{9/2} \rightarrow {}^4I_{13/2}) \sim 0.15$].

For the ($^4F_{5/2}$, $^4F_{3/2}$) and the $^2H_{9/2}$ anti-Stokes emissions, the signals were very weak. Nevertheless, some measurements could be performed by using our cw Ti:sappphire laser and an acousto-optic modulator. These transient signals were only registered to get some information about the involved up-conversion mechanisms. As shown in Fig. 8, the decay curves present a long lifetime exponential part with a time constant longer than the lifetime of the involved emitting level as obtained by resonant excitation. It simply means that, following 800 nm excitation, ETU processes take place in the three cases.

D. Low temperature measurements

Low temperature emission and excitation spectra are presented in Fig. 9. As shown in Fig. 9(a), anti-Stokes luminescences from levels $^2H_{9/2}$ and $^4F_{5/2}$ are observed, whereas no emission could be detected from level $^4S_{3/2}$. When the temperature increases, however, the intensity of this $^4S_{3/2}$ luminescence rapidly increases and becomes dominant. This observation indicates that a very efficient nonresonant energy transfer occurs between levels $^4I_{9/2}$ and $^4S_{3/2}$. Furthermore, the low temperature excitation spectra of this $^4S_{3/2}$ lumines-

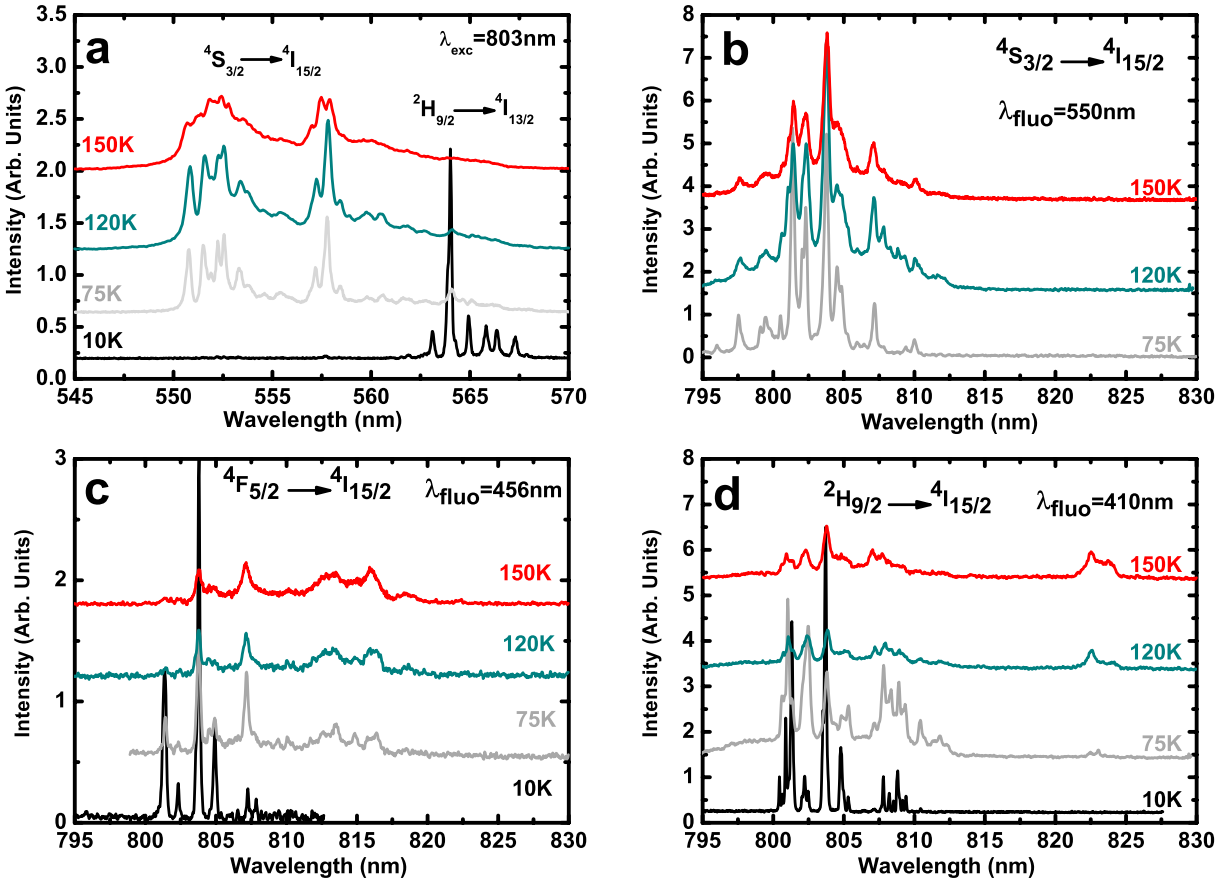

FIG. 9. (Color online) (a) Temperature evolution of the up-conversion fluorescence registered around 550 nm after 803 nm excitation. Temperature variation of the excitation spectra (recorded around 800 nm) of the up-conversion luminescences coming from the levels (b) $^4S_{3/2}$, (c) $^4F_{5/2}$, and (d) $^2H_{9/2}$.

cence [Fig. 9(b)] present some additional peaks in comparison to the excitation spectra of the $^4I_{9/2}$ luminescence (see Fig. 3). The presence of these new lines confirms that energy transfer via ESA from level $^4I_{13/2}$ to level $^2H_{11/2}$ also takes place.

The excitation spectra of $^4F_{5/2}$ as a function of temperature are presented in Fig. 9(c). At 10 K, the spectrum is very similar to the excitation spectra of the $^4I_{9/2}$ luminescence. Then, as temperature is increased, a new group of lines appears around 810–825 nm. These two groups of peaks show different temperature dependences, indicating two different origins. At low temperature, the $^4F_{5/2}$ multiplet is mainly populated via ETU processes (V) and (VI), whereas at high temperatures, ESA processes, such as process (IV) involving level $^4I_{11/2}$, also occur and increase more significantly.

Finally, in the case of the multiplet $^2H_{9/2}$, the low temperature excitation spectra are very complicated, with many additional lines compared to the $^4I_{9/2}$ excitation spectrum. This indicates that both ESA (VII) and ETU (VIII) processes take place even at low temperatures.

In conclusion of this analysis, it is demonstrated that both ESA and ETU excitation paths take place for the three kinds of studied anti-Stokes fluorescences.

E. Time-resolved measurements and determination of the energy-transfer microparameters

It was demonstrated above that pumping in the wavelength region of the $^4I_{9/2}$ absorbing level could lead to anti-Stokes luminescences coming from $^2H_{9/2}$, $^4F_{5/2}$, and $^4S_{3/2}$ resulting from ESA and ETU processes. For a more quantitative understanding of these mechanisms, knowledge of the involved downward and upward transition cross sections around 800 nm is necessary. These emission and absorption cross-section spectra for levels $^4I_{9/2}$, $^4S_{3/2}$, $^2H_{11/2}$, $^4F_{5/2}$, and $^4F_{3/2}$ have been gathered in Fig. 10.

ESA is directly evaluated with the aid of the cross section $\sigma_{\mathrm{ESA}}(\lambda)$, whereas UC energy-transfer efficiency generally requires the determination of energy-transfer microparameters noted C_{DD} and C_{DA}, as introduced first by Förster and Dexter[32,33] and very often used in the laser community.[34] These microparameters are related to the energy-transfer probability between two ions I and J separated by a distance R and given by $P_{IJ}=C_{IJ}/R^n$, where n is an integer which depends on the interaction mechanism ($n=6$ for a dipole-dipole interaction, for example). Whereas the C_{DA} microparameter stands for "static" and direct energy transfers between the same type or different ionic species, the C_{DD} one is introduced in the case of migration-type energy transfers within the same ionic species; for example, here between Er^{3+} ions in their $^4I_{9/2}$ and $^4I_{15/2}$ energy levels.

C_{DA} and C_{DD} microparameters are easily calculated once emission and ground- and excited-state absorption cross-section σ_{SE}, σ_{GSA}, and σ_{ESA} spectra have been derived by using the expressions[34]

$$C_{DA} = \frac{3c}{8\pi^4 n^2} \int \sigma_{ESA}(\lambda)\sigma_{ES}(\lambda)d\lambda \qquad (6)$$

and

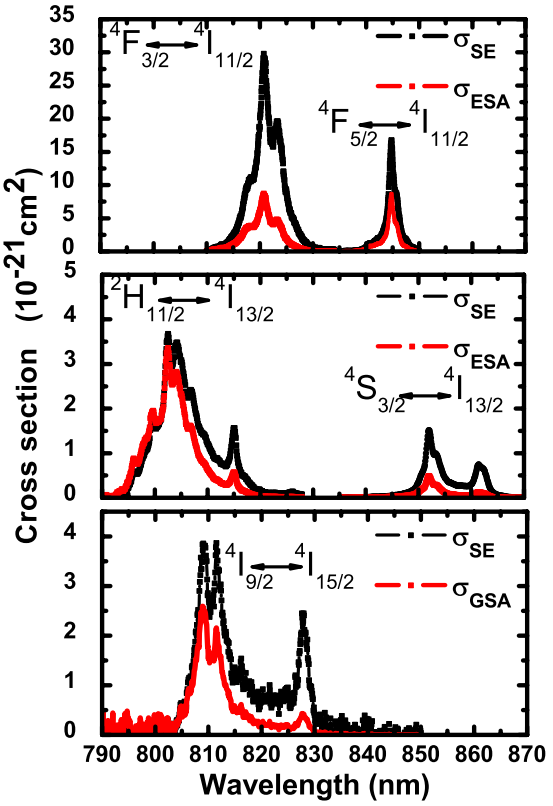

FIG. 10. (Color online) Ground-state absorption and excited-state absorption and emission cross-section spectra σ_{GSA}, σ_{ESA}, and σ_{SE}, respectively, determined around 800 nm.

$$C_{DD} = \frac{3c}{8\pi^4 n^2} \int \sigma_{GSA}(\lambda)\sigma_{ES}(\lambda)d\lambda. \qquad (7)$$

The results of these calculations, using the data reported in Fig. 10, are summarized in Table III. The microparameter values for Er^{3+}-doped oxide, fluoride, or chloride crystals usually ranges between 10^{-38} and 10^{-41} cm^6 s^{-1}.[13,34,35] Comparison between the energy-transfer microparameters of Er:KPC and Er:TPB indicates that energy transfers are less efficient in the latter host. The comparison between materials is not trivial, in fact, since the values of the energy-transfer microparameters reflect different aspects such as crystal-field splittings, transition strengths, and, in case of nonresonant energy transfer, phonon energy. If we assume nearly resonant energy transfers and similar oscillator strengths for the two hosts, the observed discrepancy between the two set of C_{DX} parameters likely comes from different crystal fields at the rare-earth ion sites, weaker in the case of TPB than in the case of KPC. This is one reason why energy-transfer microparameters between donor and acceptor C_{DA} may be smaller in Er^{3+}-doped bromides than in Er^{3+}-doped chlorides (and in fluorides and oxides): overlaps between emission and excited-state absorption spectra occur within smaller spectral regions. On the other hand, for migration-type energy transfers and associated microparameters C_{DD}, the situation may be different, since a smaller Stokes shift can favor the overlap between the involved absorption and emission spectra. So it is understandable that the observed variation of the C_{DD}

TABLE III. Comparison of experimentally derived nonradiative energy transfer microparameters of $Er:Tl_3PbBr_5$ and $Er:KPb_2Cl_5$.

	$Er:Tl_3PbBr_5$	$Er:KPb_2Cl_5$[a]	Ratio
C_{DD} $(^4I_{9/2}, {}^4I_{15/2}) \rightarrow (^4I_{15/2}, {}^4I_{9/2})$	0.95×10^{-40} cm^6 s^{-1}	1.19×10^{-40} cm^6 s^{-1}	~1.25
C_{DA} $(^4I_{9/2}, {}^4I_{9/2}) \rightarrow (^4I_{15/2}, {}^4H_{9/2})$	Not available	0.82×10^{-40} cm^6 s^{-1}	?
C_{DA} $(^4I_{9/2}, {}^4I_{11/2}) \rightarrow (^4I_{15/2}, {}^4F_{3/2})$	0.48×10^{-40} cm^6 s^{-1}	2.54×10^{-40} cm^6 s^{-1}	~5.3
C_{DA} $(^4I_{9/2}, {}^4I_{13/2}) \rightarrow (^4I_{15/2}, {}^4S_{3/2})$	0.44×10^{-40} cm^6 s^{-1}	1.00×10^{-40} cm^6 s^{-1}	~2.27

[a]Reference 13.

parameters may be less pronounced than the C_{DA} parameters.

It can be concluded that, for 800 nm excitation, optical losses induced by energy transfers will probably be less important in Er:TPB than in Er:KPC.

VI. CONCLUSION

In this paper, we have presented the optical properties of a particular Er^{3+}-doped nonhygroscopic, low-phonon-energy, and nonlinear crystal Tl_3PbBr_5. Low temperature emission and excitation spectra have been registered and analyzed to determine the list of energy levels. This analysis has proven that Er^{3+} occupy essentially one kind of crystallographic site, and a set of crystal-field parameters has been determined by assuming a C_2 site symmetry both to corroborate the observed energy levels and to give the approximate positions of others. Anti-Stokes emission and excitation spectra as well as fluorescence decays and time-resolved emission and excited-state excitation spectra have been recorded and analyzed. These data now provide all the necessary elements (such as excited-state absorption cross sections and up-conversion energy-transfer rates) for a future modeling of laser operation of the considered system under diode laser pumping using around 800 nm and to determine the effective laser potential of this Er^{3+}-doped single crystal.

ACKNOWLEDGMENTS

Thanks are expressed to DGA (Délégation Générale pour l'Armement) and CNRS (Centre National de la Recherche Scientifique) for partially supporting this work.

*alban.ferrier@ensicaen.fr

†matias.velazquez@ensicaen.fr

‡Corresponding author; richard.moncorge@ensicaen.fr

[1] S. R. Bowman, S. K. Searles, J. Ganem, and P. Smidt, in *Trends in Optics and Photonics*, edited by M. M. Fejer, H. Ingeyan, and U. Keller (Optical Society of America, Washington, D.C., 1999), Vol. 26, p. 487.

[2] S. R. Bowman, S. K. Searles, N. W. Jenkins, S. B. Qadri, and E. F. Skelton, in *Trends in Optics and Photonics*, edited by C. Marshall (Optical Society of America, Washington, D.C., 2001), Vol. 50, p. 154.

[3] R. Burlot-Loison, M. Pollnau, K. Krämer, P. Egger, J. Hulliger, and H. U. Güdel, J. Opt. Soc. Am. B **17**, 2055 (2000).

[4] K. Rademaker, W. F. Krupke, R. H. Page, S. A. Payne, K. Petermann, G. Huber, A. P. Yelisseyev, L. I. Isaenko, U. N. Roy, A. Burger, K. C. Mandal, and K. Nitsch, J. Opt. Soc. Am. B **21**, 2117 (2004).

[5] U. Hömmerich, Ei Ei Nyein, and S. B. Trivedi, J. Lumin. **113**, 100 (2005).

[6] U. N. Roy, R. H. Hawrami, Y. Cui, S. Morgan, A. Burger, K. C. Mandal, C. C. Noblitt, S. A. Speakman, K. Rademaker, and S. A. Payne, Appl. Phys. Lett. **86**, 151911 (2005).

[7] A. G. Okhrimchuk, L. N. Butvina, E. M. Dianov, N. V. Lichkova, V. N. Zagorodnev, and A. V. Shestakov, Quantum Electron. **36**, 41 (2006).

[8] A. Ferrier, M. Velázquez, X. Portier, J.-L. Doualan, and R. Moncorgé, J. Cryst. Growth **289**, 357 (2006). Note that in this paper, a misprint error occurred: we used a KDP and not a KD*P powder as a standard.

[9] H. L. Keller, Z. Anorg. Allg. Chem. **482**, 154 (1981).

[10] M. Velázquez, A. Ferrier, J.-P. Chaminade, B. Menaert, and R. Moncorgé, J. Cryst. Growth **286**, 324 (2006).

[11] A. N. Vtyurin, L. I. Isaenko, S. N. Krylova, A. Yelisseyev, A. P. Shebanin, P. P. Turchin, N. G. Zamkova, and V. I. Zinenko, Phys. Status Solidi C **1**, 3142 (2004).

[12] D. A. Pinnow, IEEE J. Quantum Electron. **6**, 223 (1970), and references therein.

[13] A. Ferrier, M. Velázquez, J. L. Doualan, and R. Moncorgé, J. Opt. Soc. Am. B **24**, 2526 (2007).

[14] A. M. Tkachuk, S. E. Ivanova, L. I. Isaenko, A. P. Yelisseyev, M. F. Joubert, Y. Guyot, and S. Payne, Opt. Spectrosc. **95**, 772 (2003).

[15] P. Dorenbos, Phys. Rev. B **62**, 15650 (2000).

[16] D. E. Mc Cumber, Phys. Rev. **136**, 954 (1964).

[17] B. F. Aull and H. P. Jensen, IEEE J. Quantum Electron. **18**, 925 (1982).

[18] B. Henderson and G. F. Imbusch, *Optical Spectroscopy of Inorganic Solids* (Oxford Science, Oxford, 1989).

[19] W. T. Carnall, P. R. Fields, and K. Rajnak, J. Chem. Phys. **49**, 4412 (1968), and references therein.

[20] C. Cascales, J. Fernandez, and R. Balda, Opt. Express **13**, 2141 (2005).

[21] C. A. Morrison and R. P. Leavitt, J. Chem. Phys. **71**, 2366 (1979).

[22] C. Rudowicz and J. Quin, J. Lumin. **110**, 39 (2004).

[23] F. Auzel and O. Malta, J. Phys. (Paris) **44**, 201 (1983).
[24] A. J. Garcia-Adeva, R. Balda, J. Fernandez, E. E. Nyein, and U. Hömmerich, Phys. Rev. B **72**, 165116 (2005).
[25] R. Balda, A. J. Garcia-Adeva, M. Voda, and J. Fernández, Phys. Rev. B **69**, 205203 (2004).
[26] V. K. Bogdanov, D. J. Booth, W. E. K. Gibbs, J. S. Javorniczky, P. J. Newman, and D. R. MacFarlane, Phys. Rev. B **63**, 205107 (2001).
[27] M. P. Hehlen, G. Frei, and H. U. Gudel, Phys. Rev. B **50**, 16264 (1994).
[28] M. Pollnau, D. R. Gamelin, S. R. Lüthi, H. U. Güdel, and M. P. Hehlen, Phys. Rev. B **61**, 3337 (2000).
[29] J. F. Suyver, A. Aebischer, S. Garcia-Revilla, P. Gerner, and H. U. Güdel, Phys. Rev. B **71**, 125123 (2005).
[30] F. Auzel, C. R. Seances Acad. Sci., Ser. B **262**, 1016 (1966).
[31] F. Auzel, Chem. Rev. (Washington, D.C.) **104**, 139 (2004).
[32] T. Förster, Ann. Phys. **2**, 55 (1948).
[33] D. L. Dexter, J. Chem. Phys. **21**, 836 (1953).
[34] J. L. Doualan, C. Maunier, D. Descamps, J. Landais, and R. Moncorgé, Phys. Rev. B **62**, 4459 (2000), and references therein.
[35] P. Le Boulanger, J. L. Doualan, S. Girard, J. Margerie, and R. Moncorgé, Phys. Rev. B **60**, 11380 (1999).